

# Protein aggregation linked to Alzheimer's disease revealed by saturation transfer MRI

Lin Chen<sup>a,b</sup>, Zhiliang Wei<sup>a,b</sup>, Kannie W.Y. Chan<sup>a,b,c</sup>, Shuhui Cai<sup>d</sup>, Guanshu Liu<sup>a,b</sup>, Hanzhang Lu<sup>a,b</sup>, Philip C. Wong<sup>e,f</sup>, Peter C.M. van Zijl<sup>a,b</sup>, Tong Li<sup>e,\*\*</sup>, Jiadi Xu<sup>a,b,\*</sup>

<sup>a</sup> F.M. Kirby Research Center for Functional Brain Imaging, Kennedy Krieger Research Institute, Baltimore, MD, USA

<sup>b</sup> Russell H. Morgan Department of Radiology and Radiological Science, The Johns Hopkins University School of Medicine, Baltimore, MD, USA

<sup>c</sup> Department of Biomedical Engineering, City University of Hong Kong, Hong Kong, China

<sup>d</sup> Department of Electronic Science, Fujian Provincial Key Laboratory of Plasma and Magnetic Resonance, Xiamen University, Xiamen, China

<sup>e</sup> Department of Pathology, The Johns Hopkins University School of Medicine, Baltimore, MD, USA

<sup>f</sup> Department of Neuroscience, The Johns Hopkins University School of Medicine, Baltimore, MD, USA

## ARTICLE INFO

### Keywords:

Chemical exchange saturation transfer (CEST)

Magnetization transfer contrast (MTC)

Alzheimer's disease (AD)

Saturation transfer (ST)

Radial acquisition

UTE-CEST

## ABSTRACT

The goal of this study was to develop a molecular biomarker for the detection of protein aggregation involved in Alzheimer's disease (AD) by exploiting the features of the water saturation transfer spectrum (Z-spectrum), the CEST signal of which is sensitive to the molecular configuration of proteins. A radial-sampling steady-state sequence based ultrashort echo time (UTE) readout was implemented to image the Z-spectrum in the mouse brain, especially the contributions from mobile proteins at the frequency offsets for the composite protein amide proton (+3.6 ppm) and aliphatic proton (−3.6 ppm) signals. Using a relatively weak radiofrequency (RF) saturation amplitude, contributions due to strong magnetization transfer contrast (MTC) from solid-like macromolecules and direct water saturation (DS) were minimized. For practical measure of the changes in the mobile protein configuration, we defined a saturation transfer difference ( $\Delta$ ST) by subtracting the Z-spectral signals at  $\pm 3.6$  ppm from a control signal at 8 ppm. Phantom studies of glutamate solution, protein (egg white) and hair conditioner show the capability of the proposed scheme to minimize the contributions from amine protons, DS, and MTC, respectively. The ST signal at  $\pm 3.6$  ppm of the cross-linked bovine serum albumin (BSA) solutions demonstrated that the  $\Delta$ ST signal can be used to monitor the aggregation process of the mobile proteins. High-resolution  $\Delta$ ST images of AD mouse brains at  $\pm 3.6$  ppm of mouse brains showed significantly reduced  $\Delta$ ST (−3.6) signal compared to the age-matched wild-type (WT) mice. Thus, this signal has potential to serve as a molecular biomarker for monitoring protein aggregation in AD.

## 1. Introduction

Alzheimer's disease (AD) is a neurological disorder that is pathologically characterized by the accumulation of neuritic plaques comprised of an amyloid-beta ( $A\beta$ ) peptide core, surrounded by dystrophic neurites, astrocytes and microglia (Hardy and Selkoe, 2002) as well as neurofibrillary tangles (NFT) composed of hyperphosphorylated tau peptide (Ballatore et al., 2007; Irvine et al., 2008; Lee and Trojanowski, 1999; Li et al., 2016; Rojas and Boxer, 2016). Early diagnosis of AD would have a

significant impact on its management and may allow for early therapeutic interventions (Baxter et al., 2007; Schenk et al., 1999; Walker and Rosen, 2006). The detection of the aggregation process of proteins involved in AD is a potential strategy for early diagnosis of the disease and is also important for dynamically monitoring the effects of new therapeutic agents on the clearance of such protein aggregates or aggregate precursors. Magnetic resonance imaging (MRI), as a non-invasive imaging technique, has been used for detailed visualization of the medial temporal lobe (MTL) structures as a core diagnostic feature

**Abbreviations:** ST, Saturation transfer; DS, Direct saturation; CEST, Chemical exchange saturation transfer; MTC, Magnetization transfer contrast; UTE, Ultrashort echo time; HS, Heat shock; AC, Anterior commissure; BSA, Bovine serum albumin; AD, Alzheimer's disease; NFT, Neurofibrillary tangles; RARE, Rapid imaging with refocused echoes; VDMP, Variable delay multiple pulse.

\* Corresponding author. Kennedy Krieger Institute, The Johns Hopkins University School of Medicine, 707 N. Broadway, Baltimore, MD, 21205, USA.

\*\* Corresponding author. Department of Pathology The Johns Hopkins University School of Medicine, 720 Rutland Avenue, Ross 558, Baltimore, MD, 21205, USA.

E-mail address: [xuj@kenedykrieger.org](mailto:xuj@kenedykrieger.org) (J. Xu).

<https://doi.org/10.1016/j.neuroimage.2018.12.018>

Received 27 July 2018; Received in revised form 8 December 2018; Accepted 10 December 2018

Available online 13 December 2018

1053-8119/© 2018 Published by Elsevier Inc.

of AD (Burton et al., 2009; Scheltens et al., 1992) but has limited molecular imaging capability because of its low detection sensitivity. Recently, significant progress has been made to visualize A $\beta$  plaques by MRI in transgenic mouse models using T<sub>2</sub> or T<sub>2</sub>\* contrast owing to the accumulation of iron in amyloid plaques (Chamberlain et al., 2009; Faber et al., 2007; Jack et al., 2004; Vanhoutte et al., 2005; Wadghiri et al., 2003; Zhang et al., 2004). However, such methods often only work in later stages of AD (Chamberlain et al., 2009; Vanhoutte et al., 2005; Zhang et al., 2004). More recent studies have employed quantitative magnetic susceptibility mapping (QSM) to show co-localization of iron and amyloid in mild cognitive impairment (MCI) (van Bergen et al., 2016). Here, we aim to develop a novel molecular biomarker for very early detection of AD using chemical exchange saturation transfer (CEST) MRI (Chen and Pagel, 2015; Liu et al., 2013; van Zijl and Yadav, 2011; Ward et al., 2000), which has emerged as a novel molecular imaging technique for detecting low-concentration metabolites and proteins (Zhou et al., 2003a, 2003b) through the water signal.

The saturation transfer (ST) spectrum (Z-spectrum) (van Zijl et al., 2018) of water has composite components from amide protons (at a frequency offset of +3.6 ppm) and aliphatic protons (relayed nuclear Overhauser enhancement or rNOE signals around −3.6 ppm) of mobile proteins (Jones et al., 2013; Ling et al., 2008; van Zijl and Yadav, 2011; Xu et al., 2014; Zaiss et al., 2017). Importantly, the line-shape of the Z-spectrum is sensitive to the molecular size and configuration of proteins (broadening with increasing size and aggregation) (Goerke et al., 2015a; Zaiss et al., 2013) and, hence, has great potential for monitoring protein aggregation in AD patients. Before the formation of plaques and tangles, both A $\beta$  and tau are relatively small molecules with rapid internal motions and molecular tumbling. These motions average out several molecular orientation-based interactions between the protons in these molecules, such as through-space dipole-dipole interaction, chemical shift anisotropy and quadrupolar interaction, the main line broadening factors in the MR spectrum. This leads to an MR spectrum and a corresponding well-defined Z-spectrum for small peptides in which the resonances of the different contributing protons can be distinguished. Once the A $\beta$  and tau monomers form oligomers and subsequent plaques and tangles, the above interactions will increase owing to the slower internal and tumbling motions, significantly broadening the spectral line-shape (Cavanagh et al., 2006; Zaiss et al., 2013). This phenomenon has been used in solutions to monitor protein folding as well as protein aggregation of A $\beta$  peptide and Huntingtin protein (Goerke et al., 2015a; Zaiss et al., 2013). However, it has yet to be verified and implemented in vivo, where many confounding factors are present. A major challenge for in vivo CEST MRI is to minimize the interferences from direct water saturation (DS) and conventional magnetization transfer contrast (MTC) induced by solid-like macromolecules in normal tissues (Helms et al., 2004; Hua et al., 2007; Levesque and Pike, 2009; Ng et al., 2009; Portnoy and Stanis, 2007; Tozer et al., 2003). In addition, high-resolution MRI is expected to be necessary for early detection of the initial burden of small plaques and tangles. In the current study, we implemented a two-dimensional ultrashort echo time (UTE) based steady-state CEST scheme (UTE-CEST) and applied this technique to monitor protein aggregation in an AD transgenic mouse model (APP<sup>swE</sup>;PS1 $\Delta$ E9 mouse). A radial acquisition scheme has been shown to have great potential for suppressing image artifacts due to motion and susceptibility differences at tissue interfaces (Du et al., 2014; Fan et al., 2018; Ma et al., 2018b; Wilhelm et al., 2012) and a similar radial MT technique with short echo time has been applied to study tissues with extremely short T<sub>2</sub> components such as Achilles tendon and cortical bone (Du et al., 2009; Ma et al., 2018a). Recently, such a scheme was also implemented for quantitative susceptibility mapping (QSM) of brain (Lu et al., 2018; Wei et al., 2018). In this paper, the method was optimized on phantoms for MTC (hair conditioner), mobile protein (egg white and cross-linked bovine serum albumin (BSA)) and glutamate (Glu) solutions, in order to verify that this technique is sensitive enough to detect protein aggregation in AD mice by measuring the differences in Z-spectral intensities between 8 ppm

reference frequency and the protein main frequencies of the composite amide (3.6 ppm) and rNOE (−3.6 ppm) signals, and comparing the differences between an AD mouse model and its healthy littermates.

## 2. Materials and methods

### 2.1. UTE-CEST sequence

The pulse sequence was composed of a train of interleaved Gaussian saturation pulses and 2D-UTE modules that implement radial acquisition as illustrated in Fig. 1A, which resembles the steady-state pulsed CEST and MTC techniques (Dixon et al., 2010; Du et al., 2009; Jones et al., 2013). Compared to its Cartesian counterpart, a radial acquisition scheme is inherently less sensitive to motion artifacts (Glover and Lee, 1995; Glover and Pauly, 1992). This advantage originates from: (i) over-sampling of the low-frequency region in k-space resulting in an averaging of artifacts, and (ii) the fact that artifacts are manifested in the form of streaks perpendicular to the direction of motion (Glover and Pauly, 1992), rather than discrete ghosts along the phase-encoding direction. Adopting the self-gating property of the radial acquisition scheme can further enhance the resistance to motion artifacts (Larson et al., 2004; Seo et al., 2017). Secondly, the radial acquisition can achieve short TE, which leads higher signal-to-noise by detecting all water components with a wide range of T<sub>2</sub> values in brain, including bound water in myelin sheets (Wilhelm et al., 2012). Compared to the other gradient echo based sequences with long TE, brain images with short TE usually show weak contrast across the brain due to the short TE and low readout flip angles applied that lead to T<sub>1</sub> or proton density weighted contrast. This allows better visualization of the pure CEST contrast due to the RF preparation scheme for CEST MRI.

The duration of the Gaussian saturation pulses was set to 30 ms with a peak B<sub>1</sub> of 0.9  $\mu$ T unless specified, and the repetition time (TR) was 40 ms. The excitation pulse for the 2D-UTE radial readout was a 0.3 ms Gaussian pulse with a peak B<sub>1</sub> of 7  $\mu$ T, which results in a flip angle of 15°. Here, a Gaussian pulse was chosen due to its small bandwidth factor (2740 Hz for a 1 ms pulse). The effective echo time (TE) was 0.3 ms. The acquisition bandwidth was 100 kHz and gradient ramp time was 100  $\mu$ s. After each saturation pulse, one radial spoke was collected. Each radial spoke was sampled from the center of k-space. In the current study, single slice CEST images were collected. The nominal Cartesian matrix size was set to 96  $\times$  96 with a resolution of 0.17  $\times$  0.17 mm<sup>2</sup> and a slice thickness of 1 mm. For half-echo acquisition mode, the number of spokes is equal to the number of nominal Cartesian phase encoding lines multiplied by  $\pi$ , i.e.,  $96^2\pi \approx 302$ . The number of sampling points is equal to half of nominal Cartesian sampling points plus 6 ramp sampling points, i.e.  $96/2 + 6 = 54$ . The total saturation time for each offset is 12 s. The width of the saturation pulse should be large enough to achieve good selectivity and minimize direct water saturation when using low B<sub>1</sub>. However, a long pulse width increases the TR and prolongs the total experimental time. In practice, we found that a 30 ms pulse width was enough to avoid the direct water saturation at the offsets of  $\pm 3.6$  ppm for a peak B<sub>1</sub> of 0.9  $\mu$ T. In vivo, although the utilization of low saturation amplitude can also significantly suppress the MTC background in the Z-spectrum, there is a small remaining effect. As demonstrated in a previous study (Chen et al., 2017), this remaining effect may cause a vertical shift of the whole Z-spectrum between mice. The problem was addressed by collecting control images at the offset of 8 ppm, while the labeling ST images were acquired with the saturation offsets at  $\pm 3.6$  ppm. Evidence for this being suitable came from MTC phantoms at this amplitude showing approximately constant MTC between 8 ppm and  $\pm 3.6$  ppm (see phantom results) (Yadav et al., 2017). The observed saturation transfer difference ( $\Delta$ ST) signals obtained by subtracting the signal intensities at 8 ppm (Z(8)) and  $\pm 3.6$  ppm (Z( $\pm 3.6$ )), i.e.,

$$\Delta ST(\pm 3.6) = Z(8) - Z(\pm 3.6) \quad (1)$$

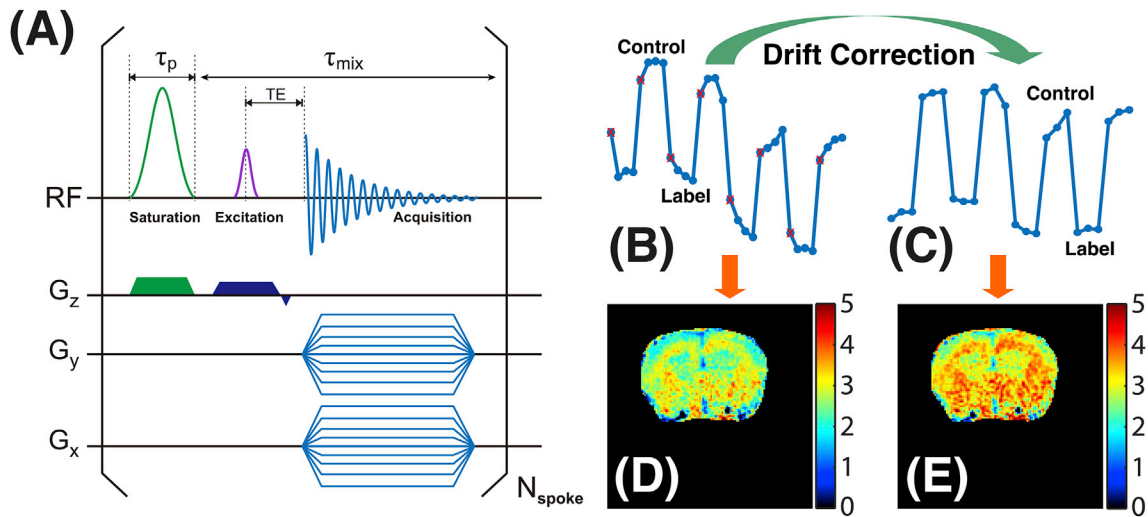


**Fig. 1.** (A) Timing diagram of the UTE-CEST sequence.  $\tau_p$  is the duration of the saturation pulses, while  $\tau_{mix}$  is the mixing time for saturation transfer between successive saturation pulses. (B–E) Flowchart of the drift correction for the  $\Delta ST$  map: (B) typical ST signal intensities as a function of time for four interleaved labeling (offset  $\pm 3.6$  ppm) and control (offset 8 ppm) images. The first data points before reaching steady state for labeling and control images are indicated by red crosses (x); (C) ST signal after drift correction. (D & E)  $\Delta ST$  maps with and without drift correction.

thus have a high degree of MTC background suppression, allowing us to focus on changes in the mobile proteins and peptides. As a comparison, the conventional ST signal at ( $\pm 3.6$ ) is defined by

$$\Delta Z(\pm 3.6) = 1 - Z(\pm 3.6) \quad (2)$$

A peak  $B_1$  of  $0.9 \mu T$  (30 ms width), corresponding to a 180-degree flip angle for the amide and aliphatic protons, theoretically can generate the highest amide and aliphatic CEST signals because the spins are inverted (Knutsson et al., 2018; Sun et al., 2008; van Zijl and Sehgal, 2016; Zu et al., 2012). Here, the flip angle for a Gaussian shaped pulse is calculated by  $\int_0^{\tau_p} \gamma B_1(t) dt$ , where  $\tau_p$  is the pulse width and  $\gamma$  the proton gyromagnetic ratio.

The signal-to-noise ratio (SNR) of the  $\Delta ST$  maps can be increased by dynamically acquiring successive labeling (offsets  $\pm 3.6$  ppm) and control (offset 8 ppm) images, calculating the difference between labeling and control images and adding them up. However, this scheme is not suitable for UTE-CEST and may lead to an underestimated value of the  $\Delta ST$  map because the magnetization cannot reach steady state in the successive labeling and control experiments. In the current study, an improved strategy was proposed inspired by the commonly used idea in fMRI (Kwong et al., 1992), i.e., a train of labeling images is interleaved with a train of control images as shown in Fig. 1B. The number of replications for labeling and control images was set to four. As shown in Fig. 1B, the first point of each labeling or control image is inaccurate owing to violation of the steady state. After the first data point, the ST signal approximately reaches a steady-state condition. In order to minimize the steady-state error of the  $\Delta ST$  maps, such first points were discarded (red crosses in Fig. 1B). In practice, this multi-label scheme may suffer from heating effects due to gradient switching and radio frequency, leading to a slow  $B_0$ -based drift in the time series data (Jones et al., 2013). This low-frequency drift in the time series data is quite similar to that in fMRI (Smith et al., 1999). The true signal can be separated from this drift by applying a high-pass frequency filter to the time series data (see the simulation in the supplemental material) (Kwong et al., 1992; Turner et al., 1998). The high-pass filter was accomplished by ‘spm\_filter’, a built-in function of SPM (<https://www.fil.ion.ucl.ac.uk/spm/software/spm12/>). There are three parameters to configure the function, i.e. the observation interval in seconds, time of observation data and cut-off period. In this study, the observation interval was set equal to the repetition time (12 s). The time of observation data was increased linearly with the step size of the observation interval. The whole acquisition time

was used as the cut-off period, which is equal to the observation interval (repetition time) multiplied by the repetition number. The  $\Delta ST$  maps are obtained by calculating the average difference between the labeling and control images.

## 2.2. Image reconstruction

Another advantage of radial acquisition is the ability for self-gating, allowing motion synchronization using the acquired MRI signals (Bonanno et al., 2018; Larson et al., 2004; Seo et al., 2017; Yang et al., 2016). The center of the k-space is repeatedly sampled in each radial spoke, of which the phase information can be used as a navigation to detect the data degraded by bulk motion. As shown in Fig. 2, motion can lead to obvious jumps in the phase navigation signal. The degraded signals acquired during motion were discarded to avoid potential motion artifacts. Non-uniform fast Fourier transform (NUFFT) is a commonly used method to reconstruct non-Cartesian MRI data (Fessler and Sutton, 2003), which consists of the following steps: density compensation, convolution and resampling, inverse FFT and apodization. The density compensation is aimed at reducing the effects of non-uniform sampling density, which can be done by multiplying the acquired radial data with the inverse density sampling function. The convolution and resampling are used to transform the non-Cartesian data into Cartesian form. The weighted radial data are convolved with a Kaiser-Bessel kernel, resampled onto a Cartesian grid. The resampled data are transformed into the image space using inverse FFT and apodization operation. The kernel size was equal to the nominal Cartesian matrix size. The kernel width and overgrid factor were set to 2 and 1.5, respectively.

The discarding of degraded spokes may lead to an under-sampled k-space and induce undesirable aliasing artifacts in the image. Compressed sensing (CS) has the ability to retrieve an aliasing free image from undersampled k-space data by exploiting the sparsity of images in the specific transform domain (Block et al., 2007; Lustig et al., 2007). In this study, CS with total variation and wavelet transforms were used to enhance the image quality. A discrete form of the CS-based Non-Uniform FFT (NUFFT) reconstruction can be described as:

$$\arg \min_x \{ \| F_n x - y \|_2^2 + \lambda_1 \| \Psi x \|_1 + \lambda_2 \| \nabla x \|_1 \} \quad (3)$$

where  $F_n$  stands for the NUFFT operation;  $x$  is the reconstructed image;  $y$  is the acquired data after motion navigation and density compensation;  $\Psi$

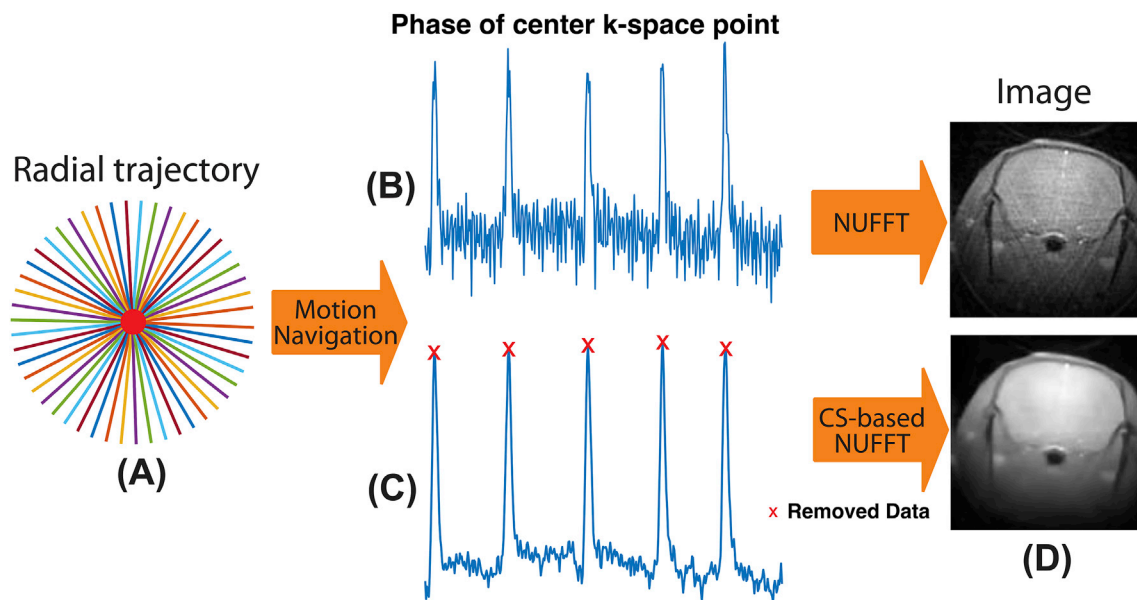


**Fig. 2.** Flowchart of image reconstruction for the radial trajectory. (A) In UTE MRI. (B) The center of  $k$ -space point is repeatedly sampled in each spoke, of which the phase can be used for the motion navigation. (C) The navigation signal is denoised and spokes affected by motion are removed. (D) The images reconstructed by NUFFT and CS-based NUFFT.

refers to the wavelet transform and  $\nabla$  stands for the finite difference transform.  $\|\cdot\|_1$  stands for the  $l_1$  norm that enhances the sparsity coefficients in the transform domain and  $\|\cdot\|_2$  stands for the  $l_2$  norm that keeps the fidelity between the reconstructed image and acquired data. The regularization parameters  $\lambda_1$  and  $\lambda_2$  control the tradeoff between sparsity and data fidelity. In practice, setting the  $\lambda_1$  and  $\lambda_2$  to  $1 \times 10^{-3}$  can always obtain a desirable result.

### 2.3. Animals

Eight animals with an age of one year were used for the current study, in which four of them were APP<sup>Swe</sup>;PS1 $\Delta$ E9 mice (Jankowsky et al., 2003) (APP mice), while another four were age-matched C57BL/6J mice (WT mice). The APP transgenic mice were bred at Johns Hopkins University and co-expressed the Swedish variant of the amyloid precursor protein (APP<sup>Swe</sup>) and the exon-9 deleted variant of presenilin1 (PS1 $\Delta$ E9). The onset of neurotic plaques in biogenic APP mice typically starts at four to six months of age (Jankowsky et al., 2003; Li et al., 2016). The image slice was located by collecting one sagittal image on the mouse brain using the RARE sequence and the position of the axial image slice was set to  $-1.4$  mm with respect to the anterior commissure (AC).

### 2.4. MRI experiments

All MRI experiments were performed on a horizontal bore 11.7 T Bruker Biospec system (Bruker, Ettlingen, Germany) equipped with actively shielded gradients, with a maximum strength of 74 Gauss/cm. For the in vivo animal MRI, a 72 mm quadrature volume resonator was used as a transmitter and a  $2 \times 2$  mouse phased array coil for acquisition. For phantoms, a 23 mm volume coil was used for both transmit and receive. All coils were from Bruker. The institutional animal care and use committee approved this study. All animals were anesthetized using 2% isoflurane in medical air, followed by 1%–1.5% isoflurane for maintenance during the MRI scan. The mouse head was positioned using a bite bar and two ear pins. During the MRI scan, mice were placed on a water-heated animal bed equipped with temperature and respiratory controls. Respiratory rate was monitored via a pressure sensor (SAII, Stony Brook, NY, USA) and maintained at 40–60 breaths per minute. The  $B_0$  field over

the mouse brain was adjusted using field-mapping and second-order shimming.

### 2.5. In vitro experiments

Two sets of phantoms (consisting of groups of 5 mm NMR tubes) were used to demonstrate the sensitivity of the UTE-CEST method for detecting protein aggregation. Egg white and hair conditioner (Suave, Estee Lauder) were selected to represent mobile protein and MTC pools, respectively. The hair conditioner contains a lamellar structure similar to membranes in neural tissues (Malyarenko et al., 2014; Varma et al., 2015). Previous studies suggest that, at low  $B_1$ , the metabolite contribution in the Z-spectrum of brain is far smaller than those from protein and lipids (Chen et al., 2017; Zu et al., 2017), and we therefore assumed the metabolite interference to the  $\Delta$ ST (3.6) signal to be negligible. A glutamate (Glu, 50 mM) phantom was used to represent amine protons in metabolites and mobile proteins that have the potential to interfere with the background of the  $\Delta$ ST (3.6) signal. Except for the hair conditioner, phantoms were prepared in phosphate buffered saline (PBS) and titrated to pH  $7.3 \pm 0.1$ .

The second series of phantoms were BSA solutions cross-linked at different temperatures to mimic protein aggregation in the brain. Tubes with BSA solution (10%w/w, pH 7.3) were incubated in heated water ( $60 \pm 1$  °C,  $65 \pm 1$  °C,  $70 \pm 1$  °C and  $80 \pm 1$  °C) for 10 min followed by placing the phantom in room temperature air for slow cooling. Once treated by this heat shock (HS), there are many types of components contained in the BSA solutions ranging from monomeric BSA to dimers, trimers and higher order polymers (Aoki et al., 1973). Hence, they can be used as a model to verify the ability of the protein  $\Delta$ ST ( $\pm 3.6$ ) signals for detecting protein aggregation.

### 2.6. In vivo UTE-CEST experiments

First, full UTE-CEST Z-spectra were acquired on WT mice to verify that the saturation amplitude of  $0.9 \mu$ T was sufficiently low to minimize the contributions of MTC and DS to the  $\Delta$ ST ( $\pm 3.6$ ) maps at 11.7 T. The saturation offset was swept from  $-15$  ppm to  $15$  ppm with peak saturation amplitudes of  $0.9 \mu$ T,  $1.2 \mu$ T and  $1.5 \mu$ T, which resulted in a total experimental time of 12 min for each saturation amplitude. The radial



readout and the duration of the saturation pulses were identical for all experiments. The UTE-CEST protocol for recording  $\Delta ST(\pm 3.6)$  maps at  $0.9 \mu T$  was used to study the age-matched APP and WT mouse groups (1 year) to verify that the  $\Delta ST(\pm 3.6)$  signal is capable of detecting protein aggregation in AD mouse brain. The  $\Delta ST(-3.6)$  map was recorded by averaging 16 images with interleaved offsets of  $-3.6$  ppm and  $8$  ppm. Each offset was repeated four times. A similar acquisition scheme was also implemented for the  $\Delta ST(3.6)$  map. The total experimental time for the  $\Delta ST(-3.6)$  or  $\Delta ST(3.6)$  maps was  $3.5$  min.

## 2.7. Quantitative magnetization transfer (qMT) experiments

The MT ratio (MTR) has been used as an overall measure of demyelination in brain, and its change has been measured for several neurologic conditions, such as mild cognitive impairment and dementia of Alzheimer's type (Bozzali et al., 2001; Kabani et al., 2002; Mascalchi et al., 2013; Ridha et al., 2007). In order to examine possible contribution of MTC effects to the  $\Delta ST(\pm 3.6)$  signal in the WT and APP mice, quantitative magnetization transfer (qMT) experiments were also performed on all APP and WT mice using the on-resonance variable delay multiple pulse (onVDMP) technique (van Gelderen et al., 2017; Xu et al., 2014, 2017). The qMT parametric maps were obtained by fitting the onVDMP buildup curves recorded using four binomial pulses ( $2$  ms,  $93.6 \mu T$ ) with five mixing times ( $0$ ,  $25$ ,  $50$ ,  $150$  and  $250$  ms). The total experimental time for the qMT experiment was  $2$  min. A two-pool model was assumed including the water and the macromolecular protons, respectively. Then, two parametric maps, the macromolecular pool to water exchange rate for the MTC pool ( $k_m$ ) and the fractional concentration of the macromolecules relative to that of the water protons ( $f_m$ ), were calculated.

## 2.8. $T_1/T_2$ relaxation time measurements

In order to examine the possible contribution of  $T_1$  and  $T_2$  relaxation times to the difference we observed in the  $\Delta ST(\pm 3.6)$  signal between WT and APP mice,  $T_1$  and  $T_2$  measurements were also performed on all mice.  $T_1$  maps were acquired using the same geometry and spatial resolution as CEST MRI using a RAREVTR sequence (RARE with variable TR =  $0.5$ ,  $1$ ,  $1.5$ ,  $2$ ,  $3.5$ ,  $5$ ,  $8$  s), while the  $T_2$  map was obtained by a multi-slice multi-echo (MSME) MRI with geometry identical to that of the  $T_1$  map measurement and an echo space of  $10$  ms.

## 2.9. Data analysis

All MRI Images were processed using custom-written MATLAB scripts (MathWorks, [www.mathworks.com](http://www.mathworks.com)). When processing the radial images, Savitzky-Golay filtering was used to smooth the phase navigation signal, which was implemented using the Matlab built-in function "sgolayfilt" with polynomial order of two and frame size of seven. A baseline correction method named BEADS (Baseline Estimation And Denoising with Sparsity) was used to remove baseline drift in the phase navigation signal (Ning et al., 2014). A local peak searching algorithm was used to find the peaks and corresponding radial spokes, which is accomplished by the Matlab built-in function "findpeaks". The degraded radial spokes were discarded to avoid potential motion artifacts. In the qMT study, a Matlab script from the literature was used for calculating the parametric maps (Xu et al., 2017). A two-sample  $t$ -test was performed between the WT and AD mice groups using the MATLAB built-in function "ttest" and was considered statistically significant for  $p < 0.05$  and highly significant when  $p < 0.001$ .

## 3. Results

### 3.1. Phantom experiments

The Z-spectra ( $S_{sat}/S_0$ ) of hair conditioner (HC), egg white and Glu solution phantoms acquired with various saturation amplitudes ( $B_1$ ) are

plotted in Fig. 3A–C, respectively. Broad Z-spectra are observed for the HC phantom (Fig. 3A) with the signal intensity at larger offsets (outside the solution proton spectral region between  $-5$  and  $5$  ppm) still not unity. The HC Z-spectra are asymmetric with respect to the water offset, an effect that becomes more apparent at higher  $B_1$  due to the quadratic increase in MTC effect with  $B_1$ . In egg white, the model for mobile proteins and peptides (Fig. 3B), the CEST signal represented by the water signal reduction due to saturation transfer  $\Delta Z$  (Eq. (2)), is observed only over the solution proton spectral range from  $-5$  ppm to  $5$  ppm. The same phenomenon is observed in the Glu solution, with a broad resonance within the range  $-1$  ppm to  $3.6$  ppm (Fig. 3C). The saturation amplitude dependent water signal reductions (Eq. (2)) at  $3.6$  ppm,  $\Delta Z(3.6)$ , for HC, egg white and Glu solution are plotted in Fig. 3D. It can be seen that the  $\Delta Z(3.6)$  for the egg white is linearly dependent on the saturation amplitude in the  $B_1$  range from  $0$  to  $2 \mu T$ , while the  $\Delta Z(3.6)$  of HC is not. The  $\Delta Z(3.6)$  of the Glu solution is negligible at saturation amplitudes below  $1.0 \mu T$ . Therefore, the contamination from the amine protons in the mobile protein  $\Delta Z(3.6)$  signal can be minimized by applying saturation amplitudes lower than  $0.9 \mu T$ . When subtracting the Z-spectral signals at  $8$  ppm and  $3.6$  ppm to obtain  $\Delta ST(3.6)$ , the values (Fig. 3E) are identical to the  $\Delta Z(3.6)$  in Fig. 3D for egg white and Glu, because of the negligible saturation for these two phantoms at  $8$  ppm. On the other hand, the  $\Delta ST(3.6)$  signal of HC is significantly smaller ( $0.7\%$  at  $0.9 \mu T$ , Fig. 3E) compared to the  $\Delta Z(3.6)$  signal ( $2.4\%$  at  $0.9 \mu T$ , Fig. 3D), which indicates that the proposed method, i.e., subtracting the signal between  $8$  ppm and  $\pm 3.6$  ppm of the Z-spectrum, can suppress the main part of the MTC contributions.

The  $\Delta ST(\pm 3.6)$  maps and mean values for the BSA phantoms before and after HS at different temperatures are illustrated in Fig. 4A–C. After the BSA protein was cross-linked, both the  $\Delta ST(3.6)$  and  $\Delta ST(-3.6)$  signals dropped significantly. The  $\Delta ST(3.6)$  values dropped from  $2.1 \pm 0.08\%$  (no HS) to  $1.2 \pm 0.08\%$  (HS at  $80^\circ C$ ) ( $P < 0.001$ ), while the  $\Delta ST(-3.6)$  values dropped from  $3.2 \pm 0.1\%$  (no HS) to  $2.0 \pm 0.1\%$  (HS at  $80^\circ C$ ) ( $P < 0.001$ ). The decrease of the  $\Delta ST(\pm 3.6)$  values as a function of HS temperature indicates that the ratio between cross-linked protein and the monomeric BSA increases as a function of the HS temperature. The  $\Delta ST(\pm 3.6)$  shows only a small difference between  $70^\circ C$  ( $\Delta ST(3.6) = 1.2\%$ ;  $\Delta ST(-3.6) = 2.1\%$ ) and  $80^\circ C$  ( $\Delta ST(3.6) = 1.2\%$ ;  $\Delta ST(-3.6) = 2.0\%$ ), which suggests that the majority of protein has already been cross-linked at  $70^\circ C$ . The typical full Z-spectra obtained by UTE-CEST MRI for the BSA phantoms before and after HS are plotted in Fig. 4D. We can see that all saturation effects for signals between  $-5$  ppm and  $5$  ppm decrease substantially after the HS. At the same time, there is an increase in broad MTC-based signal saturations at  $-8$  and  $8$  ppm induced by cross-linking the protein. These combined factors cause the significant reduction of  $\Delta ST(\pm 3.6)$  when cross-linking the protein.

### 3.2. In vivo experiments

The number of discarded spokes is related to the animal physical condition during the experiment. In our in vivo UTE-CEST experiments, it was  $68 \pm 17$ . The sampling rate after removing degraded spokes was above  $70\%$ . The signal drift due to  $B_0$  shifts during the UTE-CEST scan was found to vary significantly across mice ( $0$ – $0.8\%$  intensity change) and could be corrected well by the proposed drift correction method. Fig. 5A shows some Z-spectra recorded for the WT mice using the UTE-CEST with different saturation amplitudes, while the Z-spectra of three regions of interest (cortex, thalamus and blood vessels) are plotted in Fig. 5B. The Z value differences between  $\pm 8$  ppm ( $Z(8 \text{ ppm}) - Z(-8 \text{ ppm})$ ) are  $0.4\%$  ( $1.2 \mu T$ ) and  $1.6\%$  ( $1.5 \mu T$ ), respectively. However, at the low saturation amplitude of  $0.9 \mu T$ , the Z values at  $\pm 8$  ppm differ only about  $0.09\%$  suggesting that the MTC effect in the mouse brain is approximately symmetric for positive and negative offsets larger than  $8$  ppm or smaller than  $-8$  ppm at this amplitude. The regional Z-spectra for the cortex, thalamus, and blood are shown in Fig. 5B. It can be seen that the MTC background ( $-15$  ppm to  $-8$  ppm and  $8$  ppm– $15$  ppm) as well as the

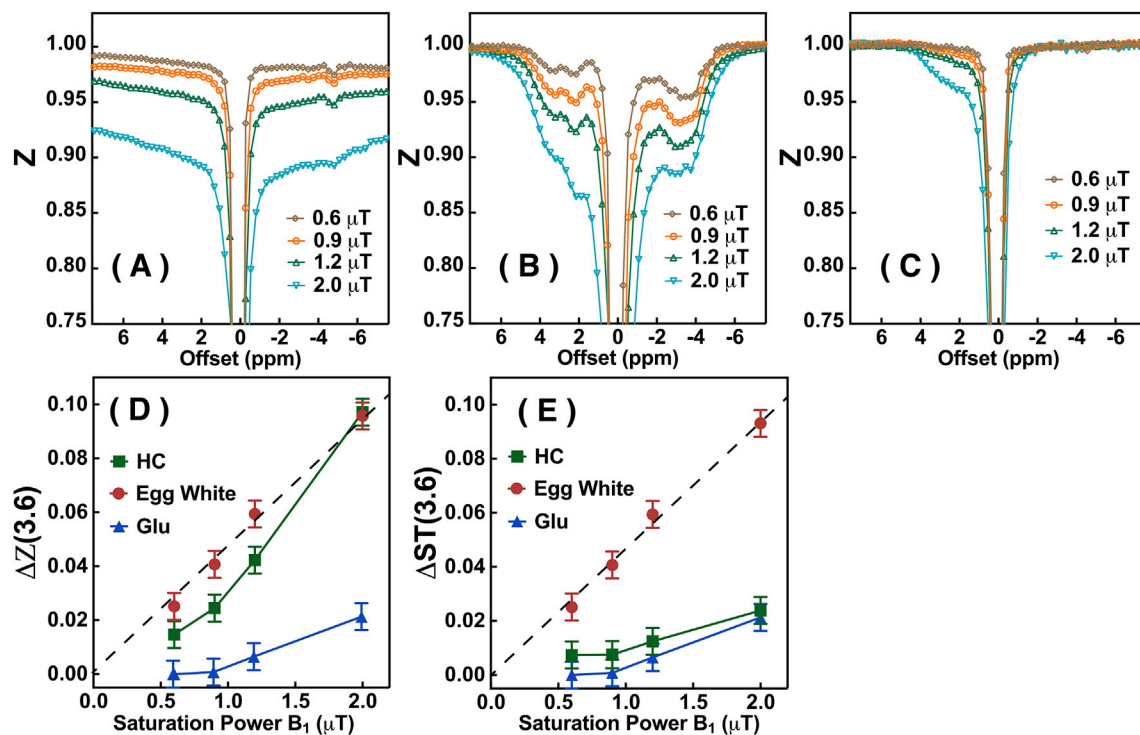


**Fig. 3.** The Z-spectra of (A) hair conditioner (HC), (B) egg white and (C) Glu solution acquired by UTE-CEST MRI with different saturation amplitudes (0.6  $\mu\text{T}$ , 0.9  $\mu\text{T}$ , 1.2  $\mu\text{T}$  and 2.0  $\mu\text{T}$ ). TR = 40 ms, TE = 0.3 ms and matrix size  $96 \times 96$  were used for the experiments. (D) The water signal reduction at 3.6 ppm ( $\Delta Z(3.6)$ ) for HC, egg white and Glu solution as a function of saturation amplitude. (E) The  $\Delta ST(3.6)$  signal of egg white, HC and Glu solution obtained by taking the signal difference between offsets 3.6 ppm and 8 ppm plotted as a function of saturation amplitude. The dashed line is a linear least square fitted curve for the  $\Delta ST(3.6)$  signal (Eq. (1)) of egg white ( $y = 0.047x$ ).

$\Delta Z(3.6)$  values are similar in the cortex and thalamus while the  $\Delta Z(-3.6)$  values differed:  $\Delta Z(-3.6) = 7.7 \pm 0.5\%$  and  $9.1 \pm 0.6\%$ , respectively. It can be seen that the  $\Delta Z$  values at 3.6 ppm, 2 ppm and  $-3.6$  ppm for blood are significantly higher than those for other tissues but have a similar shape. The observed signal in blood is known to come mainly from mobile proteins (albumin and hemoglobin) (Shah et al., 2017; Zheng et al., 2014), lending qualitative support to a large part of the in vivo signal in tissue being due to mobile proteins. In order to estimate the water signal contribution, i.e., the DS, and the water frequency, a Lorentzian line-shape was fitted to the Z-spectral points measured in the three chemical shift ranges  $-1$  ppm to  $1$  ppm,  $8$  ppm– $15$  ppm, and  $-15$  ppm to  $-8$  ppm (Fig. 5C). The contribution to the  $\Delta ST(\pm 3.6)$  from DS was found to be 0.53% for the saturation amplitude of 0.9  $\mu\text{T}$ .

Fig. 6 shows typical  $\Delta ST(\pm 3.6)$  maps for the WT and APP mice as well as representative Z-spectra from the cortex (cx) and thalamus (th). The  $\Delta ST(3.6)$  maps show weak contrast between white matter (WM) and grey matter (GM) in the brains of both WT and APP mice, which is somewhat enhanced in the APP mice. The  $\Delta ST(-3.6)$  maps of WT and APP mice both display an obvious contrast between WM and GM, but again enhanced in APP. The  $\Delta ST(\pm 3.6)$  maps of WT mice have overall higher intensity in comparison with those of the APP mice. The Z-spectra of the APP and WT mice show clear differences for both cortex and thalamus, with the Z-spectral intensity decreasing over the  $-4$  ppm to  $2$  ppm range. When comparing to the signal at  $8$  ppm there is a reduction over the  $-5$  to  $5$  ppm range, which is reflected in the maps. Notice that there are global differences in intensity across Z-spectra between WT and APP mice that appear similar to the BSA phantom data before and after heat shock. However, at low saturation amplitude, the relatively small saturation effects ( $\Delta Z(8 \text{ ppm})$ ) can be easily affected by experimental factors, such as small (a few percent) differences in the chosen ROI and slice between animals and  $B_1$  variations (see supplemental material) (Chen et al., 2017). Such effects can be on the same order of magnitude as

the change in Z ( $8 \text{ ppm}$ ) between the two types of mice. By taking the difference between the Z-spectrum intensities at  $8 \text{ ppm}$  and  $\pm 3.6 \text{ ppm}$ , most of these undesirable effects can be subtracted out, and a more robust and reliable result can be obtained.

The regional  $\Delta ST(\pm 3.6)$  values as well as Z ( $8$ ) values for the APP and WT mice are plotted in Fig. 7. The  $\Delta ST(3.6)$  values showed a large variation (range of 2–3%) for both WT and APP mice in all three brain regions studied: cortex (cx), corpus callosum (cc) and thalamus (th). The average  $\Delta ST(3.6)$  values for these three regions were found to be  $3.8 \pm 0.8\%$  (cx),  $3.8 \pm 0.6\%$  (cc) and  $4.3 \pm 1.1\%$  (th) for the WT mice and  $3.1 \pm 1\%$  (cx),  $3.4 \pm 0.8\%$  (cc) and  $3.7 \pm 1\%$  (th) for the APP mice, showing a trend of reduction but no significant effect across these three regions ( $p = 0.3$ – $0.4$ ). The  $\Delta ST(-3.6)$  values, on the other hand, were markedly different between the three brain regions with the highest values found in the thalamus ( $8$ – $11\%$ ) and the lowest values ( $4$ – $8\%$ ) in the cortex. Different from  $\Delta ST(3.6)$ , the  $\Delta ST(-3.6)$  values from APP mice were significantly lower than the corresponding values from WT mice for all brain regions ( $p \leq 0.002$ ). The Z ( $8 \text{ ppm}$ ) was found to be  $0.96 \pm 0.006$  and  $0.95 \pm 0.012$  for WT and APP mice respectively, which was not significant ( $p = 0.35$ ).

### 3.3. qMT for both WT and APP mice

Typical macromolecular fraction ( $f_m$ ) and exchange rate ( $k_m$ ) maps and the corresponding regional values for WT and APP mice are plotted in Fig. 8. The macromolecular fraction maps of cortex and thalamus displayed a strong contrast between white and gray matter, similar to the  $\Delta ST(-3.6)$  maps measured by UTE-CEST method ( $p = 0.0025$ ). However, there was no clear difference between the WT and APP mice as demonstrated by the regional values of the fraction map (Fig. 8E) ( $p = 0.71$ ). The exchange rate maps (Fig. 8C and D) also did not show clear regional differences between the two types mice (Fig. 8F).

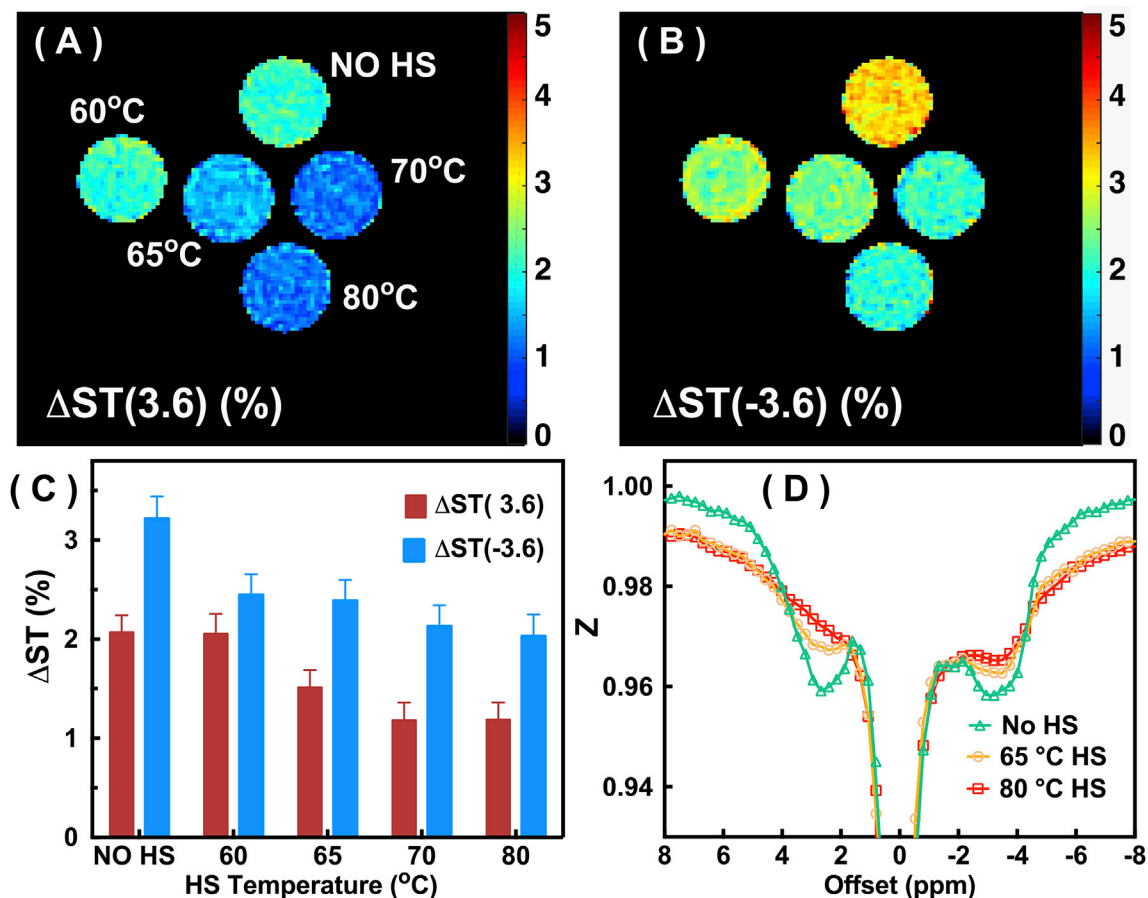


**Fig. 4.** The  $\Delta ST(3.6)$  (A) and  $\Delta ST(-3.6)$  (B) maps for the BSA solutions without heat shock (HS) (No HS) and after HS treatment at 60 °C, 65 °C, 70 °C and 80 °C. The maps were recorded using the UTE-CEST method with the parameters given in Fig. 3, and the  $\Delta ST$  values were calculated by subtracting the signals at 8 ppm and  $\pm 3.6$  ppm of the Z-spectrum. (C) The  $\Delta ST(\pm 3.6)$  values for the different tubes. (D) Z-spectra of the BSA solution before and after HS treatments (at 65 °C and 80 °C). Notice the signal reduction in the proton spectral range for mobile components and the broadening of the background signal.

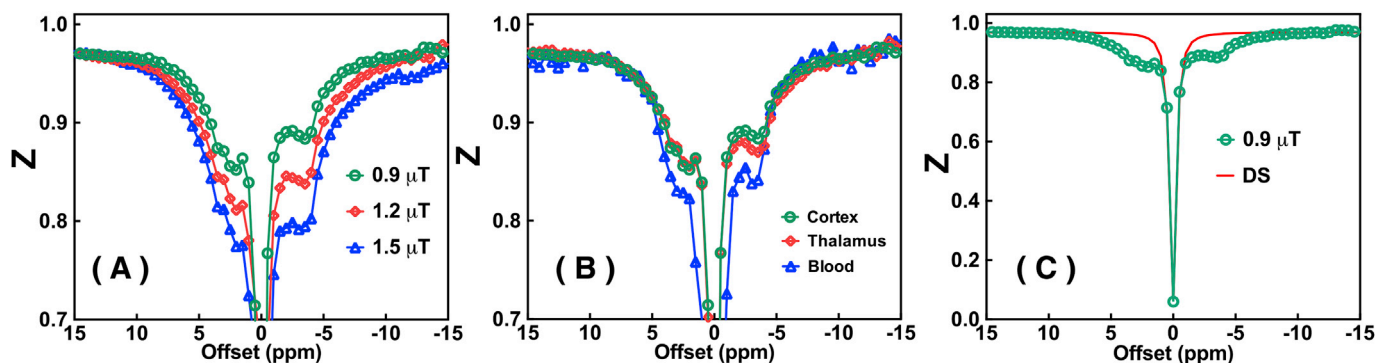


**Fig. 5.** (A) The full Z-spectra of mouse brain (cortex) recorded with peak saturation amplitudes (0.9  $\mu T$ , 1.2  $\mu T$  and 1.5  $\mu T$ ). (B) Typical Z-spectra of cortex, thalamus and blood (anterior cerebral artery, ACA) brain regions obtained with a peak saturation amplitude of 0.9  $\mu T$ . (C) The Z-spectrum of cortex recorded with saturation amplitude of 0.9  $\mu T$ , as well as water direct saturation (DS, red line) fitted using a Lorentzian line shape.

### 3.4. $T_1/T_2$ for WT and APP mice

The  $T_1$  values were found to be  $1.8 \pm 0.12$  s and  $1.7 \pm 0.12$  s for the cortex of the WT and APP mice, respectively, while the  $T_2$  values were  $35.2 \pm 0.2$  ms (WT) and  $35.6 \pm 0.5$  ms (APP). Similar to the qMT study, no clear differences were observed between WT and APP mice ( $p = 0.27$  and 0.24 for the  $T_1$  and  $T_2$  values, respectively).

### 4. Discussion

We studied the saturation transfer difference signals between 8 ppm and  $\pm 3.6$  ppm to assess protein aggregation occurring in AD. A UTE-CEST scheme with weak saturation amplitude was applied to minimize contamination by DS and MTC effects. A radial acquisition combined with retrospective motion correction and compressed sensing

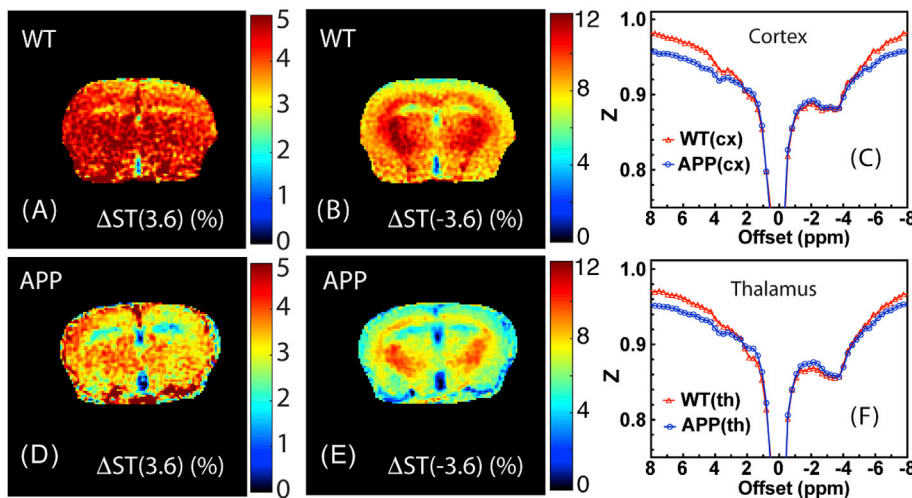


**Fig. 6.** Representative  $\Delta ST(3.6)$  maps (A, D) and  $\Delta ST(-3.6)$  maps (B, E) for the WT (A, B) and APP (D, E) mice obtained with a saturation amplitude of  $0.9 \mu T$ . The maps were recorded with 16 averages by interleaving the labeling ( $\pm 3.6$  ppm) and control (8 ppm) offsets as described in the main text. The in-plane resolution is  $0.17 \times 0.17 \text{ mm}^2$  with a slice thickness of 1 mm. The averaged Z-spectra ( $n = 2$ ) for WT and APP mice recorded with a peak  $B_1$  of  $0.9 \mu T$  for (C) cortex and (F) thalamus. Notice the broadening leading to lower intensity at the high frequency offsets as well as a reduction in saturation in the middle of the spectrum.

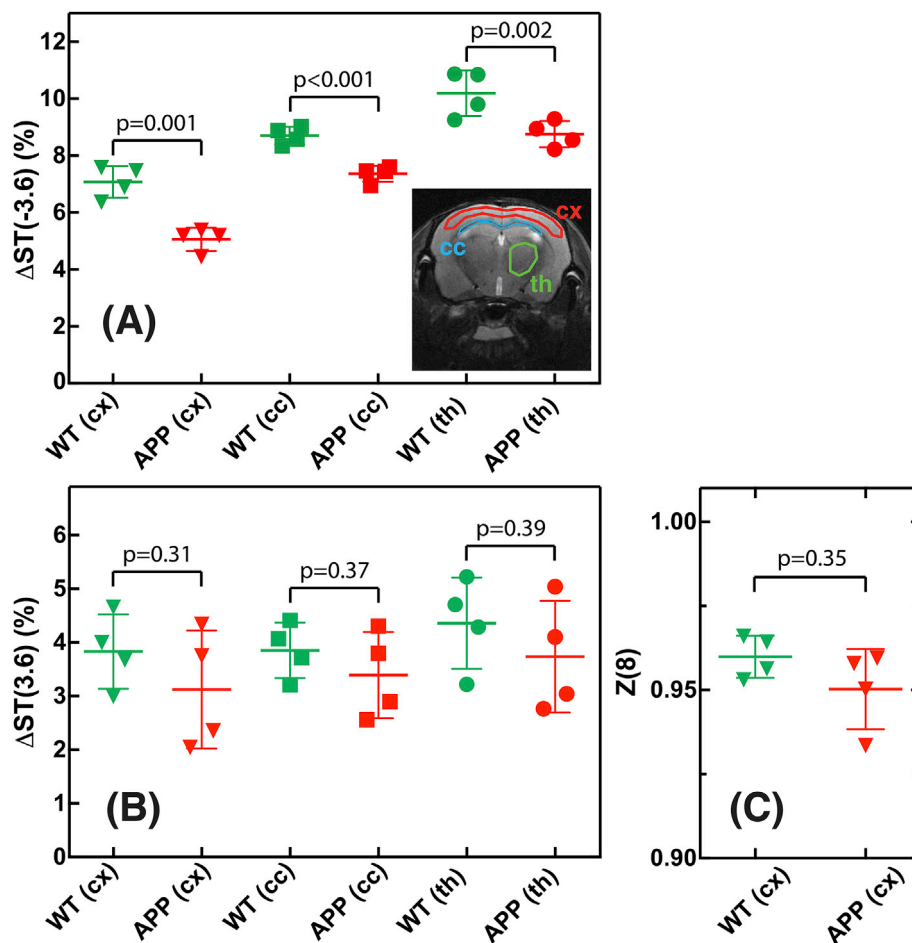


**Fig. 7.** (A,B) Comparison of  $\Delta ST(\pm 3.6)$  values between WT and APP mice for cortex (cx), corpus callosum (cc) and thalamus (th) in four mice. The image shows the location of the typical ROIs for the three brain regions. (C) Comparison of Z(8) values between WT and APP mice ( $n = 4$ ) for the cortex region.

reconstruction was used to suppress the motion artifacts induced by bulk motion and other temporal fluctuations. This allowed us to acquire high-resolution  $\Delta ST$  images at  $\pm 3.6$  ppm for mouse brains, which showed significantly reduced  $\Delta ST(-3.6)$  signal for the APP mice compared to the age-matched WT mice.

The water direct saturation in Z-spectra has been well studied previously and can be calculated with measured  $R_1$  and  $R_2$  values according

to  $R_{1\rho}$  theory (Chen et al., 2017; Jin et al., 2011; Mulkern and Williams, 1993; Zaiss and Bachert, 2013a, b). Using  $R_1 = 0.5 \text{ s}^{-1}$  and  $R_2 = 25 \text{ s}^{-1}$  (de Graaf et al., 2006), the DS contribution to the  $\Delta ST$  signal at  $\pm 3.6$  ppm can be estimated to be 0.4% for a UTE-CEST sequence with a peak saturation amplitude of  $0.9 \mu T$ . This is consistent with the value determined by fitting the Z-spectrum of the WT mice (0.53%, Fig. 5C) and is much lower than the  $\Delta ST(\pm 3.6)$  signal of the mouse brain (3–10%).



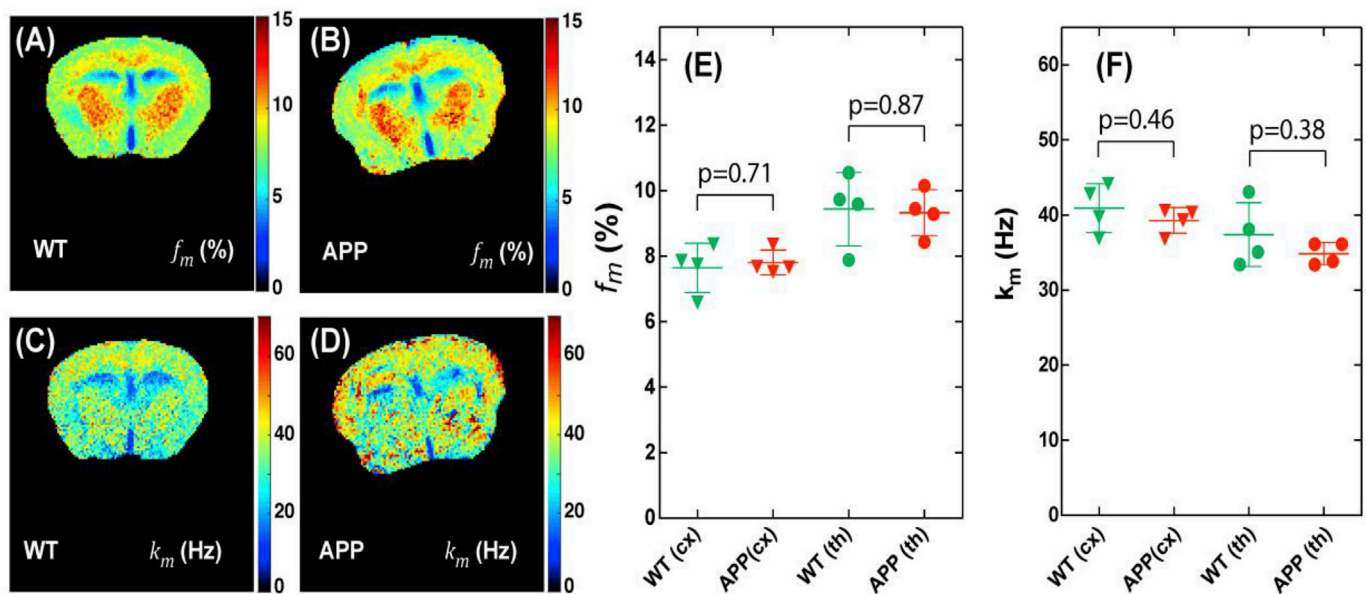


**Fig. 8.** Comparison of maps of macromolecular fraction  $f_m$  (A,B) and exchange rate  $k_m$  (C,D) for WT (A,C) and APP (B,D) mice. The in-plane resolution is  $0.17 \times 0.17 \text{ mm}^2$  with a slice thickness of 1 mm. The corresponding regional values of the macromolecular fraction (E) and exchange rate (F) for cortex (cx) and thalamus (th) in all mice studied.

Therefore, the DS contribution to  $\Delta\text{ST} (\pm 3.6)$  signal could be neglected in the current study. It should be noted that the DS contribution will be significantly increased when implementing the current method on low field scanners (see supplemental material). Then, either substantially lower saturation amplitudes are suggested to avoid the DS contamination, or a correction has to be applied. The residual MTC signal in  $\Delta\text{ST} (\pm 3.6)$  can be estimated by assuming the MTC changes to be linear with saturation offset between  $\pm 3.6 \text{ ppm}$  to  $\pm 15 \text{ ppm}$ , when using low saturation amplitudes (Desmond et al., 2014). The Z-spectra between 8 ppm and 15 ppm were used to fit such a linear function and the residual MTC contrasts at  $\pm 3.6 \text{ ppm}$  were calculated to be around  $0.66 \pm 0.22\%$ , which is far smaller than the  $\Delta\text{ST} (\pm 3.6)$  values (around 4–10%). The MTC contrast at negative frequencies can in principle be better approximated by acquiring additional UTE-CEST images with saturation offsets between  $-8 \text{ ppm}$  and  $-15 \text{ ppm}$ . However, this comes with a price of prolonging the total scan time by 50%.

The major source of the  $\Delta\text{ST} (-3.6)$  signal for the brain at lower saturation amplitudes comes from the aliphatic protons of the mobile protein and mobile lipids. Several studies by MRS and amide proton transfer (APT) based CEST MRI have shown that the protein concentration is homogenous across the brain (Snoussi et al., 2015; Xu et al., 2014, 2016). The contrast between the cortex and thalamus for the  $\Delta\text{ST} (-3.6)$  signal in the mouse brain (Fig. 6) may arise from MTC (Goerke et al., 2015b). The MTC in the mouse brain has been separated into two different components, namely fast-exchanging MTC (fast-MTC) and slow-exchanging MTC (Chen et al., 2018). The fast-MTC is symmetric with respect to the water frequency; hence, it can be well suppressed by the current MTC suppression method. On the other hand, the slow-MTC shows a maximum at around  $-3.6 \text{ ppm}$  and cannot be suppressed completely by the current scheme. The qMT studies on both mice show that the macromolecular fractions for both WT and APP mice are indistinguishable, which indicates this baseline macromolecular fraction is not sensitive to the protein aggregation. In contrast, the  $\Delta\text{ST} (-3.6)$  signal showed a much higher sensitivity in detecting differences between WT and APP, which we attribute to sensitivity in changes in mobile protein signals due to protein aggregation.

The  $\Delta\text{ST} (3.6 \text{ ppm})$  signal contains three major components: the amide protons from mobile proteins, aromatic protons (Zaiss et al., 2017) and the amine protons from mobile proteins and metabolites such as

glutamine and glutamate. Different from the  $\Delta\text{ST} (-3.6)$  signal, the  $\Delta\text{ST} (3.6)$  showed much higher variation across mice as evidenced by the coefficient of variation (CoV) for the two signals: 3.5% ( $\Delta\text{ST} (-3.6)$ ) vs 17% ( $\Delta\text{ST} (3.6)$ ) (Fig. 7). As such,  $\Delta\text{ST} (-3.6)$  should be a better biomarker in detecting protein aggregation than the  $\Delta\text{ST} (3.6)$  signal not only because of its much higher intensity, but also because of the smaller variation of the signal. However,  $\Delta\text{ST} (3.6)$  may still provide some extra information about the protein aggregation process as it does not include the lipid signal.  $\Delta\text{ST} (3.6)$  and  $\Delta\text{ST} (-3.6)$  have different sensitivity to  $B_0$  inhomogeneity. As we can see from Fig. 5B and Fig. 6 C&F, due to the broad and strong rNOE peak, the variation of ST between  $-3 \text{ ppm}$  and  $-4 \text{ ppm}$  is relatively small. On our 11.7T, the  $B_0$  inhomogeneity over the mouse brain is usually less than 0.3 ppm after shimming. Therefore, a  $B_0$  correction should not significantly affect  $\Delta\text{ST} (-3.6)$ . However, the variation of ST between 3 ppm and 4 ppm is much larger, which means  $B_0$  inhomogeneity has the potential to cause large changes in the  $\Delta\text{ST} (3.6)$  signal. As  $B_1$  can also impact the Z (8) and  $\Delta\text{ST} (-3.6)$  values (Fig. S3), it needs to be consistent among mice when performing experiments. The protein aggregation process in AD mouse is a complicated process, which may not be well mimicked by cross-linked BSA. Further studies using A $\beta$  and tau peptide aggregations or other better phantoms should be useful to further assess the origin of the  $\Delta\text{ST} (\pm 3.6)$  change.

On lower field scanners, the constant MTC background approximation between  $\pm 3.6 \text{ ppm}$  and  $\pm 8 \text{ ppm}$  is challenged by the increasing water direct saturation. To address this concern, simulations of DS contamination as a function of  $B_1$  for different field scanners were performed (see Supplementary Material). From the simulations, the proposed method should work quite well at 3T and 7T. Assuming similar DS for APP and WT mice, it should also be possible at 1.5T, where the effect could be analyzed using a full Z-spectrum and fitting out the DS (Jones et al., 2013). Another concern when transferring the method to clinical scanners is that traditional radial acquisition is relatively time-consuming compared to fast readout methods such as EPI and gradient and spin-echo (GRASE) acquisitions. This issue can be solved by using more advanced techniques, such as parallel imaging, golden angle radial acquisition and compressed sensing (Bonanno et al., 2018; Haris et al., 2017). In addition, the proposed method doesn't require the acquisition of a full Z-spectrum and there is no need to wait for full recovery of the saturation signal between successive images. Therefore, it's

possible to further shorten the total acquisition time to a clinically acceptable time.

## 5. Conclusion

The UTE-CEST technique proposed provides a simple way of acquiring high-resolution saturation transfer difference signals from mobile proteins in tissue. When comparing WT and APP mice, we found a significant decrease in  $\Delta ST$  ( $-3.6$ ) signal, which we attributed to the effect of protein aggregation involved in AD, based on comparison with phantom experiments. The  $\Delta ST$  signal may potentially be a marker for studying protein aggregation process in other diseases such as Huntington's disease and cirrhosis in the liver. However, further large-scale studies are still needed to determine the exact contributions to the  $\Delta ST$  signal decrease in AD.

## Funding

Grant support from NIH: R01EB015032, P41EB015909, R03NS109664, P50AG05146 and DOD CDMRP AZ170028.

## Acknowledgments

This work was supported by R01EB015032, P41EB015909, R03NS109664, P50AG05146 and DOD CDMRP AZ170028. Lin Chen thanks the China Scholarship Council (201506310130) for financial support.

## Appendix A. Supplementary data

Supplementary data to this article can be found online at <https://doi.org/10.1016/j.neuroimage.2018.12.018>.

## References

- Aoki, K., Sato, K., Nagaoka, S., Kamada, M., Hiramatsu, K., 1973. Heat denaturation of bovine serum albumin in alkaline pH region. *Biochim. Biophys. Acta* 328, 323–333.
- Ballatore, C., Lee, V.M., Trojanowski, J.Q., 2007. Tau-mediated neurodegeneration in Alzheimer's disease and related disorders. *Nat. Rev. Neurol.* 8, 663–672.
- Baxter, E.W., Conway, K.A., Kennis, L., Bischoff, F., Mercken, M.H., Winter, H.L., Reynolds, C.H., Tounge, B.A., Luo, C., Scott, M.K., Huang, Y., Braeken, M., Pieters, S.M., Berthelot, D.J., Masure, S., Bruinzeel, W.D., Jordan, A.D., Parker, M.H., Boyd, R.E., Qu, J., Alexander, R.S., Brennen, D.E., Reitz, A.B., 2007. 2-Amino-3,4-dihydroquinazolines as inhibitors of BACE-1 (beta-site APP cleaving enzyme): use of structure based design to convert a micromolar hit into a nanomolar lead. *J. Med. Chem.* 50, 4261–4264.
- Block, K.T., Uecker, M., Frahm, J., 2007. Undersampled radial MRI with multiple coils. Iterative image reconstruction using a total variation constraint. *Magn. Reson. Med.* 57, 1086–1098.
- Bonanno, G., Hays, A.G., Weiss, R.G., Schar, M., 2018. Self-gated golden angle spiral cine MRI for coronary endothelial function assessment. *Magn. Reson. Med.* 80, 560–570.
- Bozzali, M., Franceschi, M., Falini, A., Pontesilli, S., Cercignani, M., Magnani, G., Scotti, G., Comi, G., Filippi, M., 2001. Quantification of tissue damage in AD using diffusion tensor and magnetization transfer MRI. *Neurology* 57, 1135–1137.
- Burton, E.J., Barber, R., Mukaetova-Ladinska, E.B., Robson, J., Perry, R.H., Jaros, E., Kalara, R.N., O'Brien, J.T., 2009. Medial temporal lobe atrophy on MRI differentiates Alzheimer's disease from dementia with Lewy bodies and vascular cognitive impairment: a prospective study with pathological verification of diagnosis. *Brain* 132, 195–203.
- Cavanagh, J., Fairbrother, W.J., Palmer, A.G., Skelton, N.J., Rance, M., 2006. Protein NMR Spectroscopy Principles and Practice. Academic Press.
- Chamberlain, R., Reyes, D., Curran, G.L., Marjanska, M., Wengenack, T.M., Poduslo, J.F., Garwood, M., Jack Jr., C.R., 2009. Comparison of amyloid plaque contrast generated by T2-weighted, T2\*-weighted, and susceptibility-weighted imaging methods in transgenic mouse models of Alzheimer's disease. *Magn. Reson. Med.* 61, 1158–1164.
- Chen, L., Xu, X., Zeng, H., Chan, K., Yadav, N.N., Cai, S., Schunke, K.J., Faraday, N., van Zijl, P.C.M., Xu, J., 2018. Separating fast and slow exchange transfer and magnetization transfer using off-resonance variable delay multiple pulse (VDMP) MRI. *Magn. Reson. Med.* 80, 1568–1576.
- Chen, L., Zeng, H., Xu, X., Yadav, N.N., Cai, S., Puts, N.A., Barker, P.B., Li, T., Weiss, R.G., van Zijl, P.C.M., Xu, J., 2017. Investigation of the contribution of total creatine to the CEST Z-spectrum of brain using a knockout mouse model. *NMR Biomed.* 30, e3834.
- Chen, L.Q., Pagel, M.D., 2015. Evaluating pH in the extracellular tumor microenvironment using CEST MRI and other imaging methods. *Adv. Radiol.* 2015, 206405.
- de Graaf, R.A., Brown, P.B., McIntyre, S., Nixon, T.W., Behar, K.L., Rothman, D.L., 2006. High magnetic field water and metabolite proton T1 and T2 relaxation in rat brain in vivo. *Magn. Reson. Med.* 56, 386–394.
- Desmond, K.L., Moosvi, F., Stanisz, G.J., 2014. Mapping of amide, amine, and aliphatic peaks in the CEST spectra of murine xenografts at 7 T. *Magn. Reson. Med.* 71, 1841–1853.
- Dixon, W.T., Hancu, I., Ratnakar, S.J., Sherry, A.D., Lenkinski, R.E., Alsop, D.C., 2010. A multislice gradient echo pulse sequence for CEST imaging. *Magn. Reson. Med.* 63, 253–256.
- Du, J., Ma, G., Li, S., Carl, M., Szevenyi, N.M., VandenBerg, S., Corey-Bloom, J., Bydder, G.M., 2014. Ultrashort echo time (UTE) magnetic resonance imaging of the short T2 components in white matter of the brain using a clinical 3T scanner. *Neuroimage* 87, 32–41.
- Du, J., Takahashi, A.M., Bydder, M., Chung, C.B., Bydder, G.M., 2009. Ultrashort TE imaging with off-resonance saturation contrast (UTE-OSC). *Magn. Reson. Med.* 62, 527–531.
- Faber, C., Zahneisen, B., Tippmann, F., Schroeder, A., Fahrenholz, F., 2007. Gradient-echo and CRAZED imaging for minute detection of Alzheimer plaques in an APPV7171 x ADAM10-dn mouse model. *Magn. Reson. Med.* 57, 696–703.
- Fan, S.J., Ma, Y., Zhu, Y., Searleman, A., Szevenyi, N.M., Bydder, G.M., Du, J., 2018. Yet more evidence that myelin protons can be directly imaged with UTE sequences on a clinical 3T scanner: bicomponent T2\* analysis of native and deuterated ovine brain specimens. *Magn. Reson. Med.* 80, 538–547.
- Fessler, J.A., Sutton, B.P., 2003. Nonuniform fast Fourier transforms using min-max interpolation. *IEEE Trans. Signal Process.* 51, 560–574.
- Glover, G.H., Lee, A.T., 1995. Motion artifacts in fMRI: comparison of 2DFT with PR and spiral scan methods. *Magn. Reson. Med.* 33, 624–635.
- Glover, G.H., Pauly, J.M., 1992. Projection reconstruction techniques for reduction of motion effects in MRI. *Magn. Reson. Med.* 28, 275–289.
- Goerke, S., Zaiss, M., Kunz, P., Klika, K.D., Windschuh, J.D., Mogk, A., Bukau, B., Ladd, M.E., Bachert, P., 2015a. Signature of protein unfolding in chemical exchange saturation transfer imaging. *NMR Biomed.* 28, 906–913.
- Goerke, S., Zaiss, M., Longo, D., Garellio, F., Gregorio, E.D., Breitling, J., Ladd, M.E., Bachert, P., 2015b. CEST signals of lipids. In: 25th ISMRM. ISMRM, Honolulu, p. 0201.
- Hardy, J., Selkoe, D.J., 2002. The amyloid hypothesis of Alzheimer's disease: progress and problems on the road to therapeutics. *Science* 297, 353–356.
- Haris, K., Hedstrom, E., Bidhult, S., Testud, F., Maglaveras, N., Heiberg, E., Hansson, S.R., Arheden, H., Aletras, A.H., 2017. Self-gated fetal cardiac MRI with tiny golden angle iGRASP: a feasibility study. *J. Magn. Reson. Imag.* 46, 207–217.
- Helms, G., Dathe, H., Hagberg, G.E., 2004. Pulsed saturation of the standard two-pool model for magnetization transfer. Part II: the transition to steady state. *Concepts Magn. Reson.* 21A, 50–62.
- Hua, J., Jones, C.K., Blakeley, J., Smith, S.A., van Zijl, P.C., Zhou, J., 2007. Quantitative description of the asymmetry in magnetization transfer effects around the water resonance in the human brain. *Magn. Reson. Med.* 58, 786–793.
- Irvine, G.B., El-Agnaf, O.M., Shankar, G.M., Walsh, D.M., 2008. Protein aggregation in the brain: the molecular basis for Alzheimer's and Parkinson's diseases. *Mol. Med.* 14, 451–464.
- Jack Jr., C.R., Garwood, M., Wengenack, T.M., Borowski, B., Curran, G.L., Lin, J., Adriani, G., Grohn, O.H., Grimm, R., Poduslo, J.F., 2004. In vivo visualization of Alzheimer's amyloid plaques by magnetic resonance imaging in transgenic mice without a contrast agent. *Magn. Reson. Med.* 52, 1263–1271.
- Jankowsky, J.L., Xu, G., Fromholt, D., Gonzales, V., Borchelt, D.R., 2003. Environmental enrichment exacerbates amyloid plaque formation in a transgenic mouse model of Alzheimer disease. *J. Neuropathol. Exp. Neurol.* 62, 1220–1227.
- Jin, T., Autio, J., Obata, T., Kim, S.-G., 2011. Spin-locking versus chemical exchange saturation transfer MRI for investigating chemical exchange process between water and labile metabolite protons. *Magn. Reson. Med.* 65, 1448–1460.
- Jones, C.K., Huang, A., Xu, J., Edden, R.A., Schar, M., Hua, J., Oskolkov, N., Zaca, D., Zhou, J., McMahon, M.T., Pillai, J.J., van Zijl, P.C., 2013. Nuclear Overhauser enhancement (NOE) imaging in the human brain at 7T. *Neuroimage* 77C, 114–124.
- Kabani, N.J., Sled, J.G., Shuper, A., Chertkov, H., 2002. Regional magnetization transfer ratio changes in mild cognitive impairment. *Magn. Reson. Med.* 47, 143–148.
- Knutsson, L., Xu, J., Ahlgren, A., van Zijl, P.C.M., 2018. CEST, ASL, and magnetization transfer contrast: how similar pulse sequences detect different phenomena. *Magn. Reson. Med.* 80, 1320–1340.
- Kwong, K.K., Belliveau, J.W., Chesler, D.A., Goldberg, I.E., Weisskoff, R.M., Poncelet, B.P., Kennedy, D.N., Hoppel, B.E., Cohen, M.S., Turner, R., et al., 1992. Dynamic magnetic resonance imaging of human brain activity during primary sensory stimulation. *Proc. Natl. Acad. Sci. U.S.A.* 89, 5675–5679.
- Larson, A.C., White, R.D., Laub, G., McVeigh, E.R., Li, D., Simonetti, O.P., 2004. Self-gated cardiac cine MRI. *Magn. Reson. Med.* 51, 93–102.
- Lee, V.M., Trojanowski, J.Q., 1999. Neurodegenerative tauopathies: human disease and transgenic mouse models. *Neuron* 24, 507–510.
- Levesque, I.R., Pike, G.B., 2009. Characterizing healthy and diseased white matter using quantitative magnetization transfer and multicomponent T(2) relaxometry: a unified view via a four-pool model. *Magn. Reson. Med.* 62, 1487–1496.
- Li, T., Braunstein, K.E., Zhang, J., Lau, A., Sibener, L., Deeble, C., Wong, P.C., 2016. The neuritic plaque facilitates pathological conversion of tau in an Alzheimer's disease mouse model. *Nat. Commun.* 7, 12082.
- Ling, W., Regatte, R.R., Navon, G., Jerschow, A., 2008. Assessment of glycosaminoglycan concentration in vivo by chemical exchange-dependent saturation transfer (gagCEST). *Proc. Natl. Acad. Sci. U.S.A.* 105, 2266–2270.
- Liu, G., Song, X., Chan, K.W., McMahon, M.T., 2013. Nuts and bolts of chemical exchange saturation transfer MRI. *NMR Biomed.* 26, 810–828.

- Lu, X., Ma, Y., Chang, E.Y., He, Q., Searleman, A., von Drygalski, A., Du, J., 2018. Simultaneous quantitative susceptibility mapping (QSM) and R2\* for high iron concentration quantification with 3D ultrashort echo time sequences: an echo dependence study. *Magn. Reson. Med.* 79, 2315–2322.
- Lustig, M., Donoho, D., Pauly, J.M., 2007. Sparse MRI: the application of compressed sensing for rapid MR imaging. *Magn. Reson. Med.* 58, 1182–1195.
- Ma, Y.J., Chang, E.Y., Carl, M., Du, J., 2018a. Quantitative magnetization transfer ultrashort echo time imaging using a time-efficient 3D multispoke Cones sequence. *Magn. Reson. Med.* 79, 692–700.
- Ma, Y.J., Zhu, Y., Lu, X., Carl, M., Chang, E.Y., Du, J., 2018b. Short T2 imaging using a 3D double adiabatic inversion recovery prepared ultrashort echo time cones (3D DIR-UTE-Cones) sequence. *Magn. Reson. Med.* 79, 2555–2563.
- Malyarenko, D.I., Zimmermann, E.M., Adler, J., Swanson, S.D., 2014. Magnetization transfer in lamellar liquid crystals. *Magn. Reson. Med.* 72, 1427–1434.
- Mascalchi, M., Ginestroni, A., Bessi, V., Toschi, N., Padiglioni, S., Ciulli, S., Tessa, C., Giannelli, M., Bracco, L., Diciotti, S., 2013. Regional analysis of the magnetization transfer ratio of the brain in mild Alzheimer disease and amnesic mild cognitive impairment. *Am. J. Neuroradiol.* 34, 2098–2104.
- Mulkern, R.V., Williams, M.L., 1993. The general solution to the Bloch equation with constant rf and relaxation terms: application to saturation and slice selection. *Med. Phys.* 20, 5–13.
- Ng, M.-C., Hua, J., Hu, Y., Luk, K.D., Lam, E.Y., 2009. Magnetization transfer (MT) asymmetry around the water resonance in human cervical spinal cord. *J. Magn. Reson.* 29, 523–528.
- Ning, X.R., Selesnick, I.W., Duval, L., 2014. Chromatogram baseline estimation and denoising using sparsity (BEADS). *Chemometr. Intell. Lab. Syst.* 139, 156–167.
- Portnoy, S., Stanis, G.J., 2007. Modeling pulsed magnetization transfer. *Magn. Reson. Med.* 58, 144–155.
- Ridha, B.H., Symms, M.R., Tozer, D.J., Stockton, K.C., Frost, C., Siddique, M.M., Lewis, E.B., MacManus, D.G., Boulby, P.A., Barker, G.J., Rossor, M.N., Fox, N.C., Tofts, P.S., 2007. Magnetization transfer ratio in Alzheimer disease: comparison with volumetric measurements. *Am. J. Neuroradiol.* 28, 965–970.
- Rojas, J.C., Boxer, A.L., 2016. Neurodegenerative disease in 2015: targeting tauopathies for therapeutic translation. *Nat. Rev. Neurol.* 12, 74–76.
- Scheltens, P., Leys, D., Barkhof, F., Huglo, D., Weinstein, H.C., Vermers, P., Kuiper, M., Steinling, M., Wolters, E.C., Valk, J., 1992. Atrophy of medial temporal lobes on MRI in "probable" Alzheimer's disease and normal ageing: diagnostic value and neuropsychological correlates. *J. Neurol. Neurosurg. Psychiatry* 55, 967–972.
- Schenk, D., Barbour, R., Dunn, W., Gordon, G., Grajeda, H., Guido, T., Hu, K., Huang, J., Johnson-Wood, K., Khan, K., Kholodenko, D., Lee, M., Liao, Z., Lieberburg, I., Motter, R., Mutter, L., Soriano, F., Shopp, G., Vasquez, N., Vandever, C., Walker, S., Wogulis, M., Yednock, T., Games, D., Seubert, P., 1999. Immunization with amyloid-beta attenuates Alzheimer-disease-like pathology in the PDAPP mouse. *Nature* 400, 173–177.
- Seo, H., Kim, D., Oh, C., Park, H., 2017. Self-gated cardiac cine imaging using phase information. *Magn. Reson. Med.* 77, 1216–1222.
- Shah, S.M., Moug, O.E., Carradus, A.J., Geades, N., Dury, R., Morley, W., Gowland, P.A., 2017. The z-spectrum from human blood at 7T. *Neuroimage* 167, 31–40.
- Smith, A.M., Lewis, B.K., Ruttimann, U.E., Ye, F.Q., Sinnwell, T.M., Yang, Y., Duyn, J.H., Frank, J.A., 1999. Investigation of low frequency drift in fMRI signal. *Neuroimage* 9, 526–533.
- Snoussi, K., Gillen, J.S., Horska, A., Puts, N.A., Pradhan, S., Edden, R.A., Barker, P.B., 2015. Comparison of brain gray and white matter macromolecule resonances at 3 and 7 Tesla. *Magn. Reson. Med.* 74, 607–613.
- Sun, P.Z., Benner, T., Kumar, A., Sorensen, A.G., 2008. Investigation of optimizing and translating pH-sensitive pulsed-chemical exchange saturation transfer (CEST) imaging to a 3T clinical scanner. *Magn. Reson. Med.* 60, 834–841.
- Tozer, D., Ramani, A., Barker, G.J., Davies, G.R., Miller, D.H., Tofts, P.S., 2003. Quantitative magnetization transfer mapping of bound protons in multiple sclerosis. *Magn. Reson. Med.* 50, 83–91.
- Turner, R., Howseman, A., Rees, G.E., Josephs, O., Friston, K., 1998. Functional magnetic resonance imaging of the human brain: data acquisition and analysis. *Exp. Brain Res.* 123, 5–12.
- van Bergen, J.M., Li, X., Hua, J., Schreiner, S.J., Steininger, S.C., Quevenno, F.C., Wyss, M., Gietl, A.F., Treyer, V., Leh, S.E., Buck, F., Nitsch, R.M., Pruessmann, K.P., van Zijl, P.C., Hock, C., Unschuld, P.G., 2016. Colocalization of cerebral iron with amyloid beta in mild cognitive impairment. *Sci. Rep.* 6, 35514.
- van Gelderen, P., Jiang, X., Duyn, J.H., 2017. Rapid measurement of brain macromolecular proton fraction with transient saturation transfer MRI. *Magn. Reson. Med.* 77, 2174–2185.
- van Zijl, P.C.M., Lam, W.W., Xu, J., Knutsson, L., Stanis, G.J., 2018. Magnetization transfer contrast and chemical exchange saturation transfer MRI. Features and analysis of the field-dependent saturation spectrum. *Neuroimage* 168, 222–241.
- van Zijl, P.C.M., Sehgal, A.A., 2016. Proton chemical exchange saturation transfer (CEST) MRS and MRI. *eMagRes* 5, 1307–1332.
- van Zijl, P.C.M., Yadav, N.N., 2011. Chemical exchange saturation transfer (CEST): what is in a name and what isn't? *Magn. Reson. Med.* 65, 927–948.
- Vanhoutte, G., Dewachter, I., Borghgraef, P., Van Leuven, F., Van der Linden, A., 2005. Noninvasive in vivo MRI detection of neuritic plaques associated with iron in APP [V717I] transgenic mice, a model for Alzheimer's disease. *Magn. Reson. Med.* 53, 607–613.
- Varma, G., Duhamel, G., de Bazelaire, C., Alsop, D.C., 2015. Magnetization transfer from inhomogeneously broadened lines: a potential marker for myelin. *Magn. Reson. Med.* 73, 614–622.
- Wadghiri, Y.Z., Sigurdsson, E.M., Sadowski, M., Elliott, J.I., Li, Y., Scholtzova, H., Tang, C.Y., Aguinaldo, G., Pappolla, M., Duff, K., Wisniewski, T., Turnbull, D.H., 2003. Detection of Alzheimer's amyloid in transgenic mice using magnetic resonance microimaging. *Magn. Reson. Med.* 50, 293–302.
- Walker, L.C., Rosen, R.F., 2006. Alzheimer therapeutics-what after the cholinesterase inhibitors? *Age Ageing* 35, 332–335.
- Ward, K.M., Aletras, A.H., Balaban, R.S., 2000. A new class of contrast agents for MRI based on proton chemical exchange dependent saturation transfer (CEST). *J. Magn. Reson.* 143, 79–87.
- Wei, H., Cao, P., Bischof, A., Henry, R.G., Larson, P.E.Z., Liu, C., 2018. MRI gradient-echo phase-contrast of the brain at ultra-short TE with off-resonance saturation. *Neuroimage* 175, 1–11.
- Wilhelm, M.J., Ong, H.H., Wehrli, S.L., Li, C., Tsai, P.H., Hackney, D.B., Wehrli, F.W., 2012. Direct magnetic resonance detection of myelin and prospects for quantitative imaging of myelin density. *Proc. Natl. Acad. Sci. U.S.A.* 109, 9605–9610.
- Xu, J., Chan, K.W., Xu, X., Yadav, N., Liu, G., van Zijl, P.C., 2017. On-resonance variable delay multipulse scheme for imaging of fast-exchanging protons and semisolid macromolecules. *Magn. Reson. Med.* 77, 730–739.
- Xu, J., Yadav, N.N., Bar-Shir, A., Jones, C.K., Chan, K.W., Zhang, J., Walczak, P., McMahon, M.T., van Zijl, P.C., 2014. Variable delay multi-pulse train for fast chemical exchange saturation transfer and relayed-nuclear overhauser enhancement MRI. *Magn. Reson. Med.* 71, 1798–1812.
- Xu, X., Yadav, N.N., Zeng, H.F., Jones, C.K., Zhou, J.Y., van Zijl, P.C.M., Xu, J.D., 2016. Magnetization transfer contrast-suppressed imaging of amide proton transfer and relayed nuclear overhauser enhancement chemical exchange saturation transfer effects in the human brain at 7T. *Magn. Reson. Med.* 75, 88–96.
- Yadav, N.N., Yang, X., Li, Y., Li, W., Liu, G., van Zijl, P.C.M., 2017. Detection of dynamic substrate binding using MRI. *Sci. Rep.* 7, 10138.
- Yang, H.J., Sharif, B., Pang, J., Kali, A., Bi, X., Cokic, I., Li, D., Dharmakumar, R., 2016. Free-breathing, motion-corrected, highly efficient whole heart T2 mapping at 3T with hybrid radial-cartesian trajectory. *Magn. Reson. Med.* 75, 126–136.
- Zaiss, M., Bachert, P., 2013a. Chemical exchange saturation transfer (CEST) and MR Z-spectroscopy in vivo: a review of theoretical approaches and methods. *Phys. Med. Biol.* 58, R221–R269.
- Zaiss, M., Bachert, P., 2013b. Exchange-dependent relaxation in the rotating frame for slow and intermediate exchange – modeling off-resonant spin-lock and chemical exchange saturation transfer. *NMR Biomed.* 26, 507–518.
- Zaiss, M., Kunz, P., Goerke, S., Radbruch, A., Bachert, P., 2013. MR imaging of protein folding in vitro employing nuclear-Overhauser-mediated saturation transfer. *NMR Biomed.* 26, 1815–1822.
- Zaiss, M., Windschuh, J., Goerke, S., Paech, D., Meissner, J.E., Burth, S., Kickingeder, P., Wick, W., Bendszus, M., Schlemmer, H.P., Ladd, M.E., Bachert, P., Radbruch, A., 2017. Downfield-NOE-suppressed amide-CEST-MRI at 7 Tesla provides a unique contrast in human glioblastoma. *Magn. Reson. Med.* 77, 196–208.
- Zhang, J., Yarowsky, P., Gordon, M.N., Di Carlo, G., Munireddy, S., van Zijl, P.C., Mori, S., 2004. Detection of amyloid plaques in mouse models of Alzheimer's disease by magnetic resonance imaging. *Magn. Reson. Med.* 51, 452–457.
- Zheng, S., van der Bom, I.M., Zu, Z., Lin, G., Zhao, Y., Gounis, M.J., 2014. Chemical exchange saturation transfer effect in blood. *Magn. Reson. Med.* 71, 1082–1092.
- Zhou, J., Lal, B., Wilson, D.A., Laterra, J., van Zijl, P.C.M., 2003a. Amide proton transfer (APT) contrast for imaging of brain tumors. *Magn. Reson. Med.* 50, 1120–1126.
- Zhou, J., Payen, J.F., Wilson, D.A., Traystman, R.J., van Zijl, P.C., 2003b. Using the amide proton signals of intracellular proteins and peptides to detect pH effects in MRI. *Nat. Med.* 9, 1085–1090.
- Zu, Z., Janve, V.A., Li, K., Does, M.D., Gore, J.C., Gochberg, D.F., 2012. Multi-angle ratiometric approach to measure chemical exchange in amide proton transfer imaging. *Magn. Reson. Med.* 68, 711–719.
- Zu, Z., Louie, E.A., Lin, E.C., Jiang, X., Does, M.D., Gore, J.C., Gochberg, D.F., 2017. Chemical exchange rotation transfer imaging of intermediate-exchanging amines at 2 ppm. *NMR Biomed.* 30, e3756.